Thermal and electric field driven rf breakdown precursor formation on metal surfaces

Ryo Shinohara,[1,2,3] Soumendu Bagchi,[3,*] Evgenya Simakov,[4] Sergey V. Baryshev,[1,5] and Danny Perez[3]

[1]*Department of Electrical and Computer Engineering, Michigan State University, Michigan 48824, USA*
[2]*Department of Physics and Astronomy, Michigan State University, East Lansing, Michigan 48824, USA*
[3]*Theoretical Division, Los Alamos National Laboratory, Los Alamos, New Mexico 87545, USA*
[4]*Accelerator Operations and Technology Division, Los Alamos National Laboratory, Los Alamos, New Mexico 87545, USA*
[5]*Department of Chemical Engineering and Material Science, Michigan State University, Michigan 48824, USA*

(Received 28 November 2023; accepted 12 April 2024; published 17 May 2024)

The phenomenon of electric breakdown poses serious challenges to the design of devices that operate in high electric field environments. Experimental evidence points toward breakdown events that are accompanied by elevated temperatures and dark current spikes, which is attributed to high-asperity nanostructure formation that enhances the local electric field and triggers a runaway process. However, the exact mechanistic origin of such nanostructures under typical macroscopic operational conditions of electric field and magnetic-field-mediated heating remains poorly understood. In this work, we simulate the evolution of a copper surface under the combined action of the electric fields and elevated temperatures. Using a mesoscale curvature-driven surface evolution model, we show how a copper surface can undergo a type of dynamical instability that naturally leads to the formation of sharp asperities in realistic experimental conditions. Exploring the combined effect of fields and temperature rise, we identify the critical regimes that allow for the formation of breakdown precursors. The results show that thermoelastic stresses, while not essential, can significantly lower the critical electric field required for runaway surface instability, which is consistent with experimental observations that thermal effects can increase breakdown rates.

DOI: 10.1103/PhysRevAccelBeams.27.053101

I. INTRODUCTION

Application of high electric field is commonplace in modern vacuum technologies ranging from the space propulsion to powerful linear accelerators [1,2]. In this latter use case, next-generation radiofrequency (rf) accelerator technologies aim to operate at electric fields exceeding 100 MV/m [3,4]. However, high-field accelerators are susceptible to spontaneous vacuum arcing launched by so-called breakdown (BD) events. Breakdowns and arcs not only perturb normal operation but also cause damages to the devices, ultimately limiting the maximum attainable fields. In spite of the fact that the occurrence of BD has been known for over a century, the detailed mechanism behind BD nucleation and evolution remain poorly understood, in great part because BD events occur on the nanoscale and destroy their precursors.

Previous experimental, theoretical, and computational efforts [5–9] have proposed essential processes, categorizing them into two major groups: (i) processes that lead (i.e., nucleate) to the formation of BD events and (ii) processes that take place during the BD event, including its terminal stage. It is hypothesized that BD likely nucleates through the formation of geometrical submicron (i.e., nanoscale) asperities. These asperities can locally enhance the applied field, triggering a runaway process that eventually leads to material evaporation and terminal arc formation. However, the exact mechanisms behind the formation of such nanostructures on initially mirror-quality polished surface remain subject to speculation. While microscopic details remain poorly understood, a number of factors are known to strongly affect the breakdown rate (BDR), including applied electric fields, microstructural variations, alloying, [2], and temperature/pulse heating [10–12]. While reducing the temperature decreases the BDR [10], increasing the operating temperature above room temperature by only

*Present address: Center for Nanophase Materials Sciences, Oak Ridge National Laboratory, Oak Ridge, TN 37831, USA.

50 K can quickly increase the BDR and essentially limit the practical fields [10,11]. When not actively cooled, the operating temperature of cavity walls, being exposed to rf pulses, can also grow due to Joule heating [13], thereby producing cyclic temperature rises and affecting the BDR [2]. These facts suggest that electric and magnetic fields can act synergistically to enhance breakdown propensity beyond what would be expected from the application of a strong electric field alone, as would be the case in direct current (dc) systems. This observation can be rationalized by the fact that many rf devices, such as multicell standing/traveling wave accelerating cavities, often (and by design) exhibit significant spatial overlap between regions of high magnetic and electric fields [14–17]. This further indicates that many rf structures will contain regions that experience simultaneous exposure to high surface fields and pulsed heating, leading to a potentially complex interplay between the two (electrical and thermal) driving forces. Investigating this interplay and its effect on the BD precursor formation is the main objective of this paper.

Previous analyses have demonstrated how metallic surfaces can evolve under high electric field alone [18–21]; however, the synergy between electric field and thermoelastic stresses remains, to our knowledge, unexplored. Here, we consider the surface diffusion as a possible mechanism enabling the formation of BD precursors under nominal experimental conditions. By considering the competition between surface tension and the external electric and thermomechanical driving forces, we show that thermoelastic stresses arising from pulsed heating can assist the formation of BD precursors by lowering the critical E field for runaway surface instabilities as compared to dc field scenarios/conditions [6] where thermoelastic stresses are not expected to play a significant role.

II. PROBLEM FORMULATION

We consider 2D domains that contain a vacuum and an elastic half-space that here corresponds to bulk copper (Fig. 1). In this domain, surface evolution is assumed to follow from surface diffusion driven by electrostatic, thermoelastic, and surface energy contributions.

A. Electrostatics analysis

In order to determine the local electric field (E) along the materials surface, we solve for the electrostatic potential (ϕ) using Gauss's law in the domain shown in Fig. 1 under an applied electric field (E_a):

$$\nabla \cdot (\nabla \phi) = 0. \tag{1}$$

The material (copper) is idealized as a perfect conductor where the electric potential vanishes, enforcing Dirichlet boundary condition at the copper/vacuum interface. At a large enough distance away from the material surface, we employ Neumann boundary conditions where the field is constrained to the nominal applied field E_a. Once Eq. (1) is solved, the electric field at any position can be obtained by taking the negative gradient of the potential $-\nabla\phi = E$. Although the main motivation of our model is to capture surface evolution in the context of rf breakdown, the applied field is kept constant during the simulation, since the timescale for surface morphology evolution is much slower than that of an rf cycle (of roughly 100 ps in X-band). In this context, we can assume effective dc-field conditions at the surface corresponding to the rms of an rf cycle.

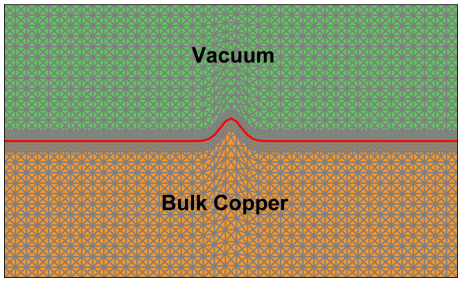

FIG. 1. Example of FEM mesh used for the simulation where the vacuum medium is shown as the green mesh and the bulk copper material is shown here as orange. The red line shows the vacuum-copper boundary.

B. Thermoelasticity analysis

To capture the effects of rf losses, we model the elastic deformation in the copper domain resulting from a uniform temperature rise. Such uniform temperature approximation stems from the fact that the high thermal conductivity of copper rapidly equilibrates temperature gradients over the micron length scales simulated here. Indeed, experiments with rf pulse heating show that temperature gradients tend to form on the scale of mm to cm [22], which is consistent with our assumption.

The governing equations for small deformations on isotropic and homogeneous materials can be written as in Refs. [23,24]:

$$-\nabla \cdot \sigma(u) = 0, \tag{2a}$$

$$\sigma(u) = \lambda \mathrm{tr}(\epsilon(u))\mathbb{1} + 2\mu\epsilon(u) - \frac{\alpha Y}{1-2\nu}\Delta T\mathbb{1}, \tag{2b}$$

$$\epsilon(u) = \frac{1}{2}(\nabla u + (\nabla u)^T), \tag{2c}$$

where σ is the stress tensor, u is the displacement vector, ϵ is the infinitesimal strain tensor, λ and μ are the Lamé's elasticity parameters, α is the thermal expansion coefficient, Y is the Young's modulus, ν is the Poisson's ratio, and ΔT is the temperature change from the reference temperature (here 300 K).

We use fixed displacement boundary conditions at the bottom of the domain and periodic boundary conditions along the lateral boundaries. The solution of Eq. (2a) produces the displacement vector field u describing the deformation of the material under a given ΔT. With the displacement vector, the corresponding strain and stress tensors can be obtained from Eqs. (2b) and (2c), respectively.

It is important to note that the thermoelasticity only acts as a driving force for surface evolution if the system is partially mechanically constrained, preventing relaxation to a stress-free configuration. In an rf setting, where heating from Joule losses mainly affects the surface region (at skin depth), confinement is provided by the bulk of the material which remains colder and hence at a shorter lattice constant. In the present study, periodic boundary conditions mimic such mechanical constraint by restricting lateral thermal expansion (but not perpendicular to the surface, which is free to relax outward). This greatly reduces the numerical cost by avoiding the simulation of a large volume of material whose only role is to impose mechanical confinement.

C. Surface diffusion

We incorporate material transport through a surface diffusion process, where the diffusion flux (J) is proportional to the surface field of the chemical potential (μ_c) as

$$J = -\frac{D_s}{k_b T}\frac{\partial \mu_c}{\partial s}, \tag{3}$$

where D_s is surface diffusivity, k_b is the Boltzmann constant, T is the absolute temperature, and derivative with respect to s is evaluated along the surface.

From mass conservation, the normal velocity V_n of the surface can be expressed using the surface divergence of $-J$. V_n can then be reformulated in terms of $\partial h(x,t)/\partial t$, the vertical velocity of the surface profile. The latter can be written as [25,26]

$$V_n = \frac{D_s \Omega v_s}{k_b T}\frac{\partial^2 \mu_c}{\partial s^2}, \tag{4a}$$

$$\frac{\partial h}{\partial t} = \frac{D_s v_s \Omega}{k_B T}\frac{\partial}{\partial x}\left[(1+h_x')^{-1/2}\frac{\partial}{\partial x}(\mu_c)\right]. \tag{4b}$$

Here h_x' indicates the derivative with respect to x, and v_s is the number of atoms per unit area.

Aggregating the contribution of electrostatics, thermoelastic stresses, and surface tension, the chemical potential on the surface can be written as [25]

$$\begin{aligned}
\mu_c &= \Omega(\gamma\kappa + \omega_T - U_E),\\
\kappa &= -\frac{h_x''}{(1+h_x'^2)^{3/2}},\\
\omega_T &= \frac{1}{2}\left(\sum_{j=1}^{2}\sum_{i=1}^{2}\sigma_{ij}\epsilon_{ij}\right),\\
U_E &= \frac{1}{2}\epsilon_0 E_{\text{local}}^2.
\end{aligned} \tag{5}$$

Here, ω_T is the strain-energy density function for linear isotropic materials, U_E is the electric field-energy density on the material's surface, γ is the isotropic surface free energy, and κ is the local surface curvature. The surface field-energy density and the strain-energy density are calculated simultaneously on their respective mesh, and Eq. (4b) is solved to calculate the vertical velocity of the surface. The meshes for the vacuum and material domains are then updated to conform at the new interface. The field and thermal stress is recalculated again for each domain after approximately 100 time steps, when the surface has evolved by a sufficient amount. This frequency is adjusted depending on the geometry and the surface velocity. The open source PDE solver FEniCS [27] was used to solve the governing equations using the finite-element method. Variational forms are specified in the FEniCS workflow in the high-level Python-based Unified Form Language [28]. These forms are then automatically compiled and executed through high-performance computational kernels using the finite-element library DOLFIN [29]. This computational approach was incorporated in a framework called SurFE-XD (Surface curvature-driven Finite Elements model for Diffusion under eXtreme conditions, previously introduced to investigate the electric-field-driven surface evolution [18]). This framework is here generalized through the addition of thermoelastic driving forces.

D. Initial surface morphology

We consider three different types of surface geometries: isolated perturbations, sinusoidal perturbations, and random surfaces. An example of isolated perturbation is shown in Fig. 1 where the simulated initial profile is modeled by a Gaussian on an otherwise flat surface. For sinusoidal surfaces, the material's surface is perturbed by a perfect sine wave with constant wavelength λ commensurate with the lateral size of the domain. For both Gaussian and sinusoidal surfaces, the aspect ratio of the perturbation is defined as the ratio of the height over either two lateral standard deviation (for isolated perturbations) or the wavelength (for sinusoidal perturbations) of the respective initial surface profile.

Finally, random surfaces were used to capture the evolution of realistic copper surfaces. In this case, the vacuum-copper boundary was represented as a sum of Fourier modes [30]:

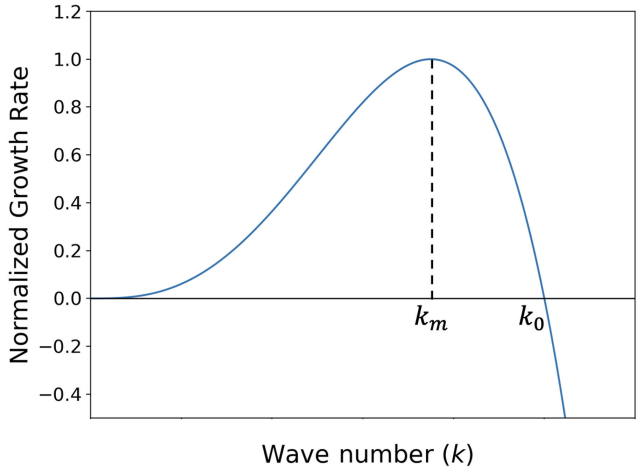

FIG. 2. Growth rate $g(k)$ for surface wave number k. Perturbations with wave number $k < k_0$ will grow, while those corresponding to larger wave numbers will decay. The maximum growth rate occurs at $k = k_m$. See text for details.

$$h(x) = \sum_n^N A_n \sin(n\omega x + \phi_n), \tag{6}$$

where the amplitude A_n is obtained by fitting an exponential decay law to an experimentally measured spatial frequency spectrum of electropolished copper photocathodes [31] and the phases ϕ_n are sampled randomly.

E. Linear stability analysis

Linear stability analysis can be used to complement fully nonlinear numerical solutions by providing analytical solutions in the limit of small perturbations. This provides analytical guidelines and serves as a baseline verification of the numerical results.

By inserting Eq. (5) into Eq. (4b) and assuming a small initial perturbation $h(x) = h_0 \sin(kx)$, the solution in the frequency domain takes the form of $h(k,t) = h_0 \exp(g(k)t)$, where $g(k)$ is the growth rate corresponding to wave number k. In the small perturbation regime, Eq. (5) can be simplified as $\kappa \approx \frac{\partial^2 h}{\partial x^2} = -Ak^2 \sin(kx)$, $U_E = \epsilon_0 E_0^2[k \sin(kx)]$, $\omega_T = 2kY\alpha^2\Delta T^2$, resulting in the temporal surface evolution described as [32,33]

$$\frac{\partial h}{\partial t} = C[-\gamma h_x'''' - k h_x''(2\alpha^2\Delta T_0^2 Y - \epsilon_0 E_0^2)], \tag{7a}$$

$$h(t,k) = h_0 \exp\left[C(2k^3\alpha^2\Delta T_0^2 Y + \epsilon_0 E_0^2 k^3 - \gamma k^4)t\right], \tag{7b}$$

where $C = \frac{D_s v_s \Omega^2}{k_B T}$.

Figure 2 reports the growth rate $g(k) = C(2k^3\alpha^2\Delta T_0^2 Y + \epsilon_0 E_0^2 k^3 - \gamma k^4)$. The result shows that perturbations corresponding to wave number below a critical value $k_0 = 1/\gamma(2\alpha^2\Delta T_0^2 Y + \epsilon_0 E_0^2)$ will grow, while larger wave number modes will decay. The fastest growing mode can be found by solving $\partial g(k)/\partial k = 0$, which gives $k_m = 3k_0/4$. The result indicates that the maximally unstable mode k_m and critical mode k_0 both depend quadratically on the operating/applied field and temperature rises. In general, higher temperatures or applied fields allow for the spontaneous growth of perturbations at increasingly large wave numbers (increasingly small wavelengths). For typical applied field of 100 MV/m and $\Delta T = 100$ K, the critical wavelength, $\lambda_0 = 2\pi/k_0$, is approximately 12 μm. If the field increases to 300 MV/m, λ_0 decreases to 6 μm.

Equation (7b) can also be used to approximate small amplitude surface evolution by taking the Fourier transform of the equation. The critical temperature rise, T_{cr}, and the critical nominal field, E_{cr}, can be defined using this approximation by finding the value in which linear stability approximation predicts a zero growth velocity. It is important to note that this approximation is only expected to hold for small perturbations, as interactions between modes are not taken into account by this approach.

III. RESULTS

A. Effect of heating

In the following, the temporal evolution of the modeled surface profiles is reported in dimensionless time τ. Conversion to physical time units will be discussed in Sec. IV. We first consider the evolution of a copper surface subjected to a uniform temperature rise in the absence of applied electric fields [25]. The results of a uniform temperature rise of 120 K applied to a sinusoidal surface are shown in Fig. 3. A temperature rise in the bulk material results in compressive stresses due to the material being constrained in the lateral direction. The resulting deformation causes the strain-energy density to be concentrated at the trough of the sinusoidal profile, resulting in sharpening of the troughs and simultaneous broadening of the peaks.

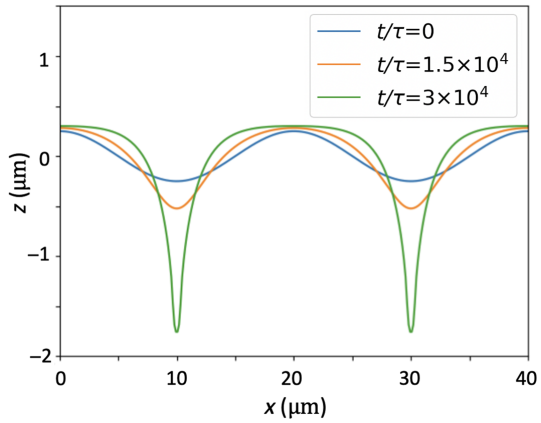

FIG. 3. Simulated copper surface profile after applying a 120 K uniform temperature rise to an initial sinusoidal perturbation.

These concomitant sharpening and broadening occur due to conservation of mass during the surface diffusion: the material removed from the trough is redistributed to the surroundings of the original maxima. This is a key point—the evolution of a small amplitude perturbation dominated by temperature rise alone is unlikely to drive the formation of a type of precursor that would lead to breakdown, as flat peaks and sharp troughs do not couple efficiently with an electric field in a way that is expected to cause runaway field emission. Electric fields are therefore expected to be a critical ingredient in the formation of BD precursors.

B. Effect of electric field

In contrast, the application of sufficiently large electric fields has been shown to lead to runaway tip growth and sharpening, due to the localized enhancement of electric fields in regions of high negative curvatures [18]. Similar mechanisms drive the formation of Taylor cones in liquid conductors [34] as well as on metal electrode surfaces [35,36]. Therefore, field driven evolution of small-amplitude perturbations initially present on the metal surface is a likely candidate for the formation of sharp asperity breakdown precursors. Note that, in contrast to the case of heating, grooving instabilities were not observed under the electric field alone.

C. Critical *E* field and heating regimes for instability

In order to unveil the synergistic effect between the two driving forces, i.e., a combined thermal and electric field effects, we conducted series of simulations by applying electric field ranging from 140 to 275 MV/m and temperature rise ranging from 0 to 100 K to act on a surface profile having an aspect ratio ranging from 0.1 to 1.5. Here, the initial asperity has a Gaussian profile with a 2 standard deviation width of 10 μm.

Figure 4(a) reports a phase diagram of simulations with different combinations of aspect ratio, applied field, and temperature rise. Here, the color scale represents the time at which either the surface grows by 10% of its initial height or reaches instability (c.f., Fig. 2). The black points represent the simulations in which the temperature rise and electric field were not sufficient to lead to growth, resulting in the initial protrusion to decay back toward a flat surface. The black dashed lines and the colored lines in Fig. 4(a) separate these two regimes but should not be taken as the precise location of the actual boundary, given the limited number of simulations. It has to be emphasized that the phase diagram reported here corresponds to a particular initial perturbation width of 10 μm. As discussed in Sec. II E, broader perturbations would decrease the critical fields, while narrower perturbations would increase them. Further analysis of these factors can be found in Sec. III D.

At small aspect ratios [0.1 (red) and to a lesser extent 0.5 (green)], temperature and applied electric field display synergistic effects, causing tip growth in a regime where

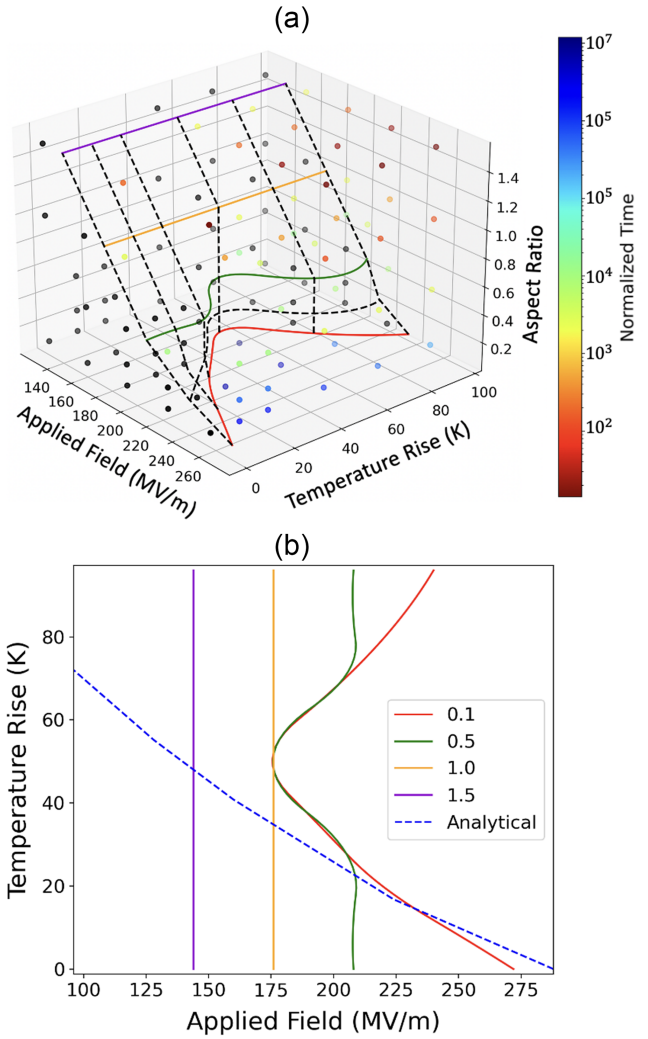

FIG. 4. (a) Phase diagram showing the normalized time at which an initial surface profile grows by 10% of the original height or reaches instability for given combination of parameters. (b) Interpolated horizontal slice of the phase diagram at various aspect ratios with analytically predicted boundary for low aspect ratio.

electric fields alone would be subcritical. This behavior is initially captured by the linear stability analysis introduced in Sec. II E above (blue dotted line), within the uncertainty of the exact location of the boundary. As the temperature rises above a certain value (about 55 K), the trend reverses and heating contributes less and less to the formation of breakdown precursors. In contrast, at higher aspect ratios (≥ 1), the propensity for BD precursor formation is unaffected by heating.

Note that high amounts of heating alone do not lead to BD, as it instead leads to grooving instabilities with blunt peaks, as described above. The resulting reduction in peak (negative) curvature creates microstructures that couple weakly with the electric field and hence to the absence of tip growth. Therefore, breakdown would not be expected in the high-*T*/low-*E* regime, in agreement with the observations reported in Fig. 4.

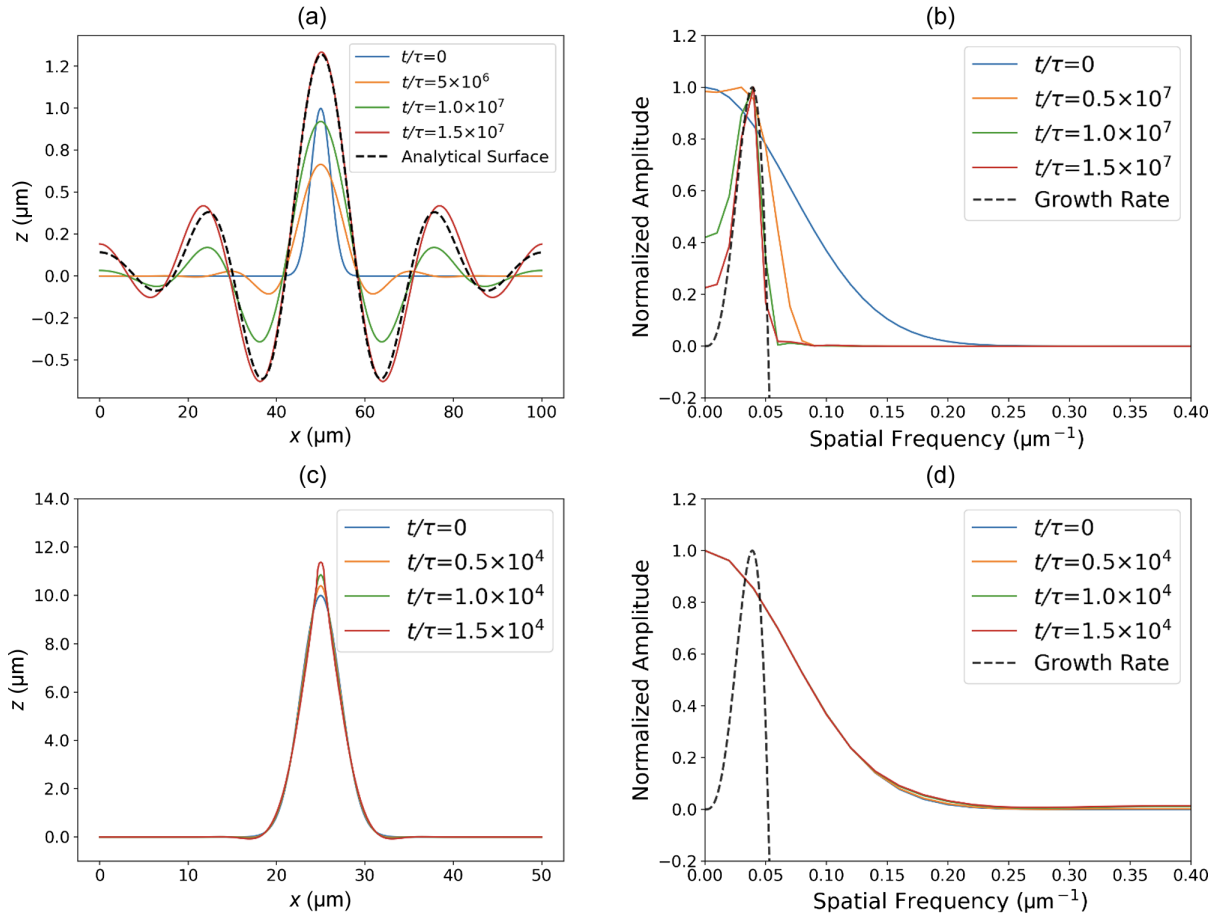

FIG. 5. (a) Surface evolution with 48 K temperature rise, 192 MV/m, and 0.1 aspect ratio. (c) Surface evolution with 48 K, 192 MV/m, and 1.0 aspect ratio. (b), (d) Fourier transform of the surface profile from the FEM simulations (c) with analytical growth rate curve calculated from Eq. (7b).

The opposite regime, high-E/low-T has been previously investigated [18]. In this case, the critical electric field required for instability was shown to decrease with aspect ratio, i.e., as a consequence of the fact that the electric field enhancement factor at the tip is proportional to the aspect ratio. This effect is observed in Fig. 4, as expected.

On general grounds, one might also expect that heating would not affect tip growth at high aspect ratio, as the elastic energy due to thermal loading can be efficiently relaxed given that the material is then not efficiently laterally constrained at the tip (in contrast to bulk materials or low aspect ratio asperities). In this limit, BD propensity can be expected to be unaffected by heating. This is again consistent with the results shown in Fig. 4.

The intermediate regime of E and T at low aspect ratio is more complex. Figure 5(a) illustrates a surface profile for a simulation with initial aspect ratio of 0.1 under application of a field of 192 MV/m and a temperature rise of 48 K. This corresponds to conditions where BD would not have been expected under this electric field alone; heating is therefore enhancing BD precursor formation in this case. The analytical solution of Eq. (7b) under this small surface perturbations is plotted against the simulation results. The agreement is excellent, thereby showing that the emerging wavelength, shown in Fig. 5(b), follows the predictions of linear stability analysis. Additionally, the spectral analysis in Fig. 5(b) illustrates the strong selection of a particular surface wavelength corresponding to the maximum of the predicted growth rate $g(k)$ for the applied parameters combination. This amplification process is efficient as the initial surface profile has a significant amplitude at that frequency. Higher frequency modes are quickly suppressed, leading to efficient wavelength selection. The mode amplitude obtained computationally is in excellent agreement with the analytically predicted growth rate. Analytically, the fastest growing mode $k_m/(2\pi)$ is predicted for a wavelength of 0.039 μm^{-1}, compared to 0.04 μm^{-1} observed in the simulations. When the aspect ratio is much higher, (1.0, which is a case that would be expected to experience BD under the corresponding electric field alone), Figs. 5(c) and 5(d) show that wavelike surface evolution with a strong wavelength selection does not occur (at least initially). Instead, high-frequency modes are amplified by coupling with the E field at the tip, leading

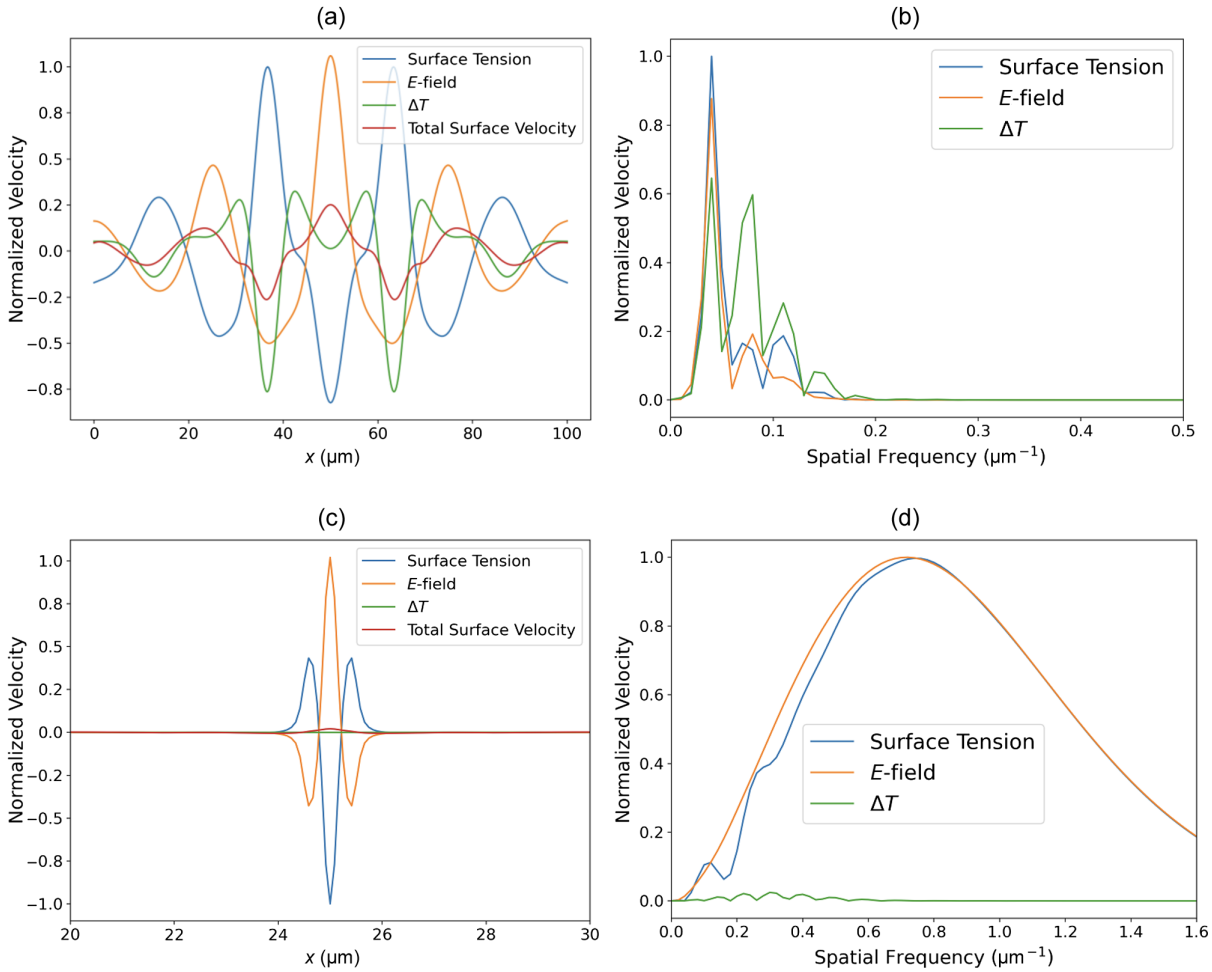

FIG. 6. (a) Velocity components of the final surface profile shown in Fig. 5(a) for surface tension, applied electric field, and temperature rise. The applied parameter for the simulations are 0.1 aspect ratio, 48 K temperature rise, and 192 MV/m. (c) Velocity component for simulation with 1.0 aspect ratio., 48 KΔT, 192 MV/m. (b), (d) Fourier transform of the individual velocity components, respectively, for the final surface in (a) and (c).

to rapid tip growth and sharpening, and ultimately to BD. As shown by the comparison to the analytically predicted growth rates (dashed line), the evolution at high-aspect ratio cannot be described by the linear perturbation and is instead dominated by nonlinear effects caused by the large curvature at the tip, which leads to the growth of high-frequency modes.

In order to elucidate the mechanics behind the surface evolution in a coupled setting, it is useful to isolate the surface velocity contributions stemming from surface tension, electric field, and heating. Such a summary is reported in Figs. 6(a) and 6(c) for two aspect ratios, 0.1 and 1.0.

The surface tension contribution (blue line) is observed to counteract any curvature: when negative curvature develops (at tips), the surface tension's contribution is negative, leading to blunting, but when the curvature is positive (at grooves), the surface tension component is positive, again leading to blunting. In contrast, the electric field contributions (orange line) tend to amplify both tips and grooves, as the material diffuses along the field gradient (from grooves, where the applied field is partially shielded, toward tips where the field is amplified). Finally, heating (green lines) tends to amplify grooves much more than tips, as discussed above. At low aspect ratios, the velocity contributions from each driving forces are similar. At higher aspect ratios, corresponding to Fig. 6(d), the relative contribution from heating is marginal compared to the surface and electric field components, consistent with the above discussion that thermoelasticity couples weakly with tiplike structures, in contrast to electric fields that are strongly amplified at such features [18]. In this case, the surface evolution is only weakly affected by heating, consistent with the results shown in Fig. 4.

Electric fields, therefore, provide the main driving force leading to the increase in negative curvature necessary for BD to occur. Nonetheless, Fig. 4 clearly shows that thermoelastic driving forces can assist with tip growth when acting concurrently with an electric field. At low heating, the observed enhancement follows the predictions

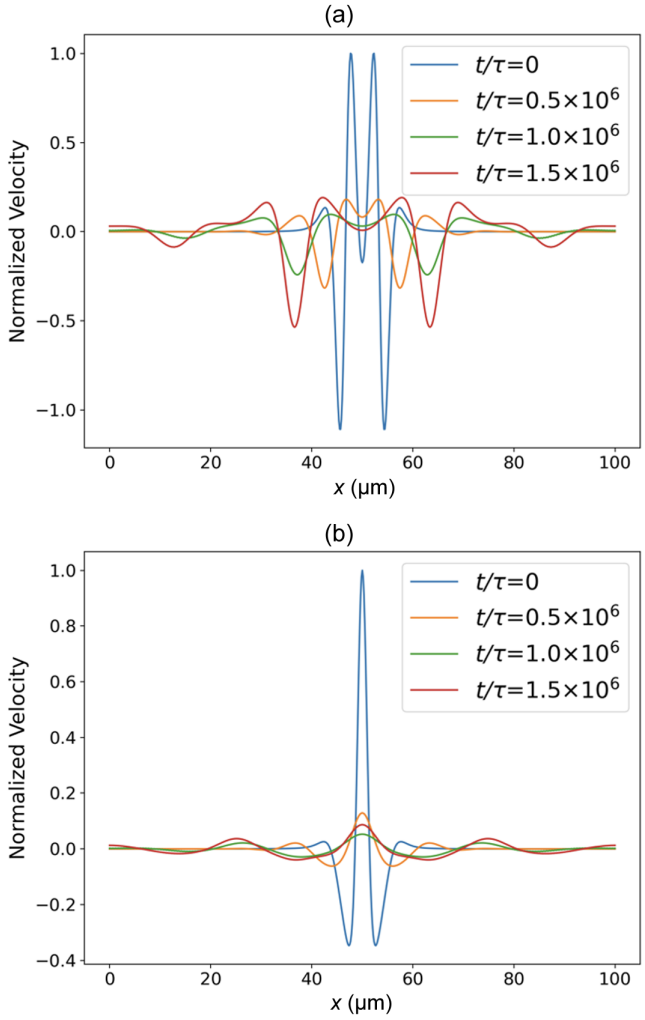

FIG. 7. Velocity contribution from (a) temperature rise and (b) applied field at various t/τ for the surfaces shown in Fig. 5(a).

of the analytic linear perturbation model. This suggests that the main effect in this case is the amplification of the growth rate of high-frequency modes that are required for the eventual creation of sharp features that efficiently couple with the electric field to cause BD. This is confirmed in Fig. 7(a), where it can be seen that thermoelasticity contributes a relatively small but positive velocity at the tip location at short times. As the aspect ratio of the asperity increases, this velocity component correspondingly decreases as expected.

As the temperature increases further, the trend reverses and the assistance provided by heating becomes less significant. Departure from the linear-stability predictions suggests that nonlinear/large-deformation effects are responsible for this reversal. The behavior observed for strong heating in Fig. 3 shows that runaway groove growth, which forms in the nonlinear, large amplitude regime, leads to a blunting of the tip region. The fact that the location of the initial tip moved up during surface evolution shows that blunting resulted from the mass flowing out of the groove and not primarily from surface tension (which would have pulled the tip region down). The same effect appears to be responsible for the decrease in assistance provided by a large amounts of heating with respect to BD formation at small aspect ratio. Our simulations show that if runaway groove growth sets in before tip growth, the mass flowing out of the grooves contributes to a decrease in the curvature in the tip region that hampers the sharpening of the tip, hence leading to a relative decrease in the efficiency of the coupling with the electric field and a relative decrease of BD propensity. Note that even beyond the turnover point, thermoelasticity still contributes to a decrease in the critical electric field for BD, although this enhancement is lessened for very large temperature rises.

D. Random surface simulation

The analysis above focused on isolated perturbations. In realistic surfaces, roughness will initially be present on a wide range of scales and wavelengths. In the following, realistic surface profiles were generated using the amplitude/wavelength characteristics measured on actual copper photocathode surfaces after electropolishing [31].

An electric field of 460 MV/m and a temperature rise ΔT of 130 K were applied on the copper surface. The observed growth behavior remains consistent with the linear stability analysis (c.f., Fig. 8): the evolution of the frequency spectra shows the preferential growth of the maximally unstable frequency modes predicted by linear stability analysis, while high-frequency modes above the critical frequency $k/2\pi > k_0/2\pi$, sharply decay, again in accordance with the analytical predictions [Fig. 8(b)]. This leads to a form of wavelength selection that promotes the growth of a relatively narrow band of wavelengths.

Figure 8(c) charts the evolution of maximally unstable wavelength λ_m against different combinations of applied fields and ΔT. The significant variation λ_m, which can vary by almost a factor of 1000 in a range of experimentally relevant parameters suggests that consistent wavelength selection would constitute a strong experimental signature of the effects discussed here.

IV. DISCUSSION

The simulations presented above suggested that surface diffusion can be an effective mechanism that contributes to breakdown precursor formation. To predict the physical timescale over which this mechanism can be expected to occur, the simulation time unit (τ) can be related to physical times as follows:

$$\tau = \frac{k_b T}{\gamma D_s v_s \Omega^2}. \tag{8}$$

The main unknown in this conversion factor is the effective diffusivity of copper atoms on surfaces, which, on clean surfaces, is of the form $D_s = 3.615^2/2 \times 10^{12} \exp(-E_b/k_b T)$ Å^2/s [37], where E_b is the migration

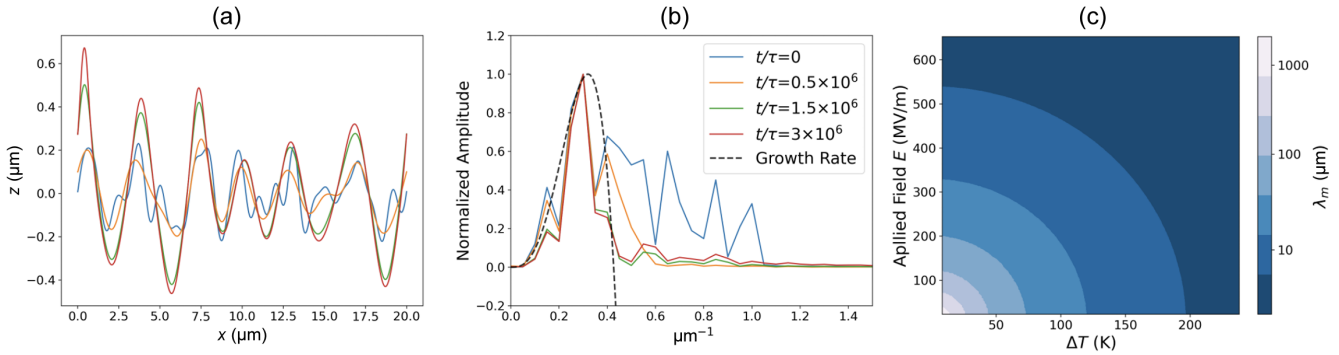

FIG. 8. Surface evolution of a random surface under application of electric field and temperature rise of 460 MV/m and 130 K, respectively. The initial surface structure was initialized following the frequency content observed experimentally for electro-polished copper surfaces [31].(b) Fourier transforms of the surface profiles superimposed with the linear-stability growth rate $g(k)$. The t/τ legend applied to both figure (a) and (b). (c) Log scale contour plot showing the fastest growing wavelength λ_m for given combination of applied field and ΔT.

barriers, and a standard prefactor of $10^{12}/\mathrm{s}$ was assumed. According to both the experimental and theoretical calculation, the migration barriers vary considerably for different surface orientations: 0.1–0.15 eV for (111), 0.25–0.30 eV for (110), and 0.38–0.69 eV for (100) [38–43]. Using $\gamma = 1.5\ \mathrm{J/m^2}$ [44], $\Omega = 11.81\ \text{Å}^3$, and $v_s = 0.306\ \text{Å}^{-2}$ [45], this wide range of possible diffusivities translates into a broad range of physical timescales τ varying from 4.75 ms ($E_b = 0.1$ eV) to 11 s ($E_b = 0.3$ eV) with room temperature. Due to the exponential dependence of the diffusivity with temperature, a temperature rise can significantly decrease the timescale, e.g., with ΔT of 100 K, the characteristic timescale vary from 2.4 ms ($E_b = 0.1$ eV) to 0.81 s ($E_b = 0.3$ eV). Further, the growth rates of perturbations can vary by orders of magnitude depending on the applied fields and temperature rises, as shown in Fig. 4. From the linear stability analysis described above, one can indeed show that the growth rate of the maximally unstable mode will increase as $\mathcal{O}[\exp[-E_b/k_b(T+\Delta T_0)](E_0^2+\Delta T_0^2)^4]$. This is qualitatively consistent with the dramatic acceleration of the breakdown rate with increasing field and temperature observed in the literature [2], where it was observed to scale with applied field to a large power [46]. Nonlinearities due to high-aspect ratios are expected to further increase the breakdown rates [18].

Our results are consistent with a number of experimental observations. First, the peak pulse heating temperature is known to be strongly correlated with the breakdown rate in rf applications [2]. This is consistent with the synergistic effect observed in this study and with the exponential increase in surface transport rates. Second, it could be expected that breakdown precursors would develop faster on surface orientations where adatom transport is faster. Indeed, it was found by electron backscattering diffraction measurements of conditioned Cu samples [22] exposed to cyclic pulsed heating (without a significant electric field applied), that the resulting surface roughness was heavily dependent on the orientations of the surface. The surface orientation with the largest damage/roughness development was observed to be (111), followed by (110), and finally by (100), which corresponds to increasing order of surface migration energy E_b, which is qualitatively consistent with the mechanism discussed here. We, however, note that this specific experiment was carried out under conditions of thermal cycling, so other mechanism (e.g., the formation of shear bands) could have contributed to the development of surface roughening.

V. CONCLUSION

This manuscript reports on a numerical model describing how metallic surfaces undergo tip-growth instabilities through surface diffusion under applied electric fields assisted by thermoelastic stresses, a situation which can be expected to be present in a number of rf devices. Such instabilities can naturally lead to the formation of geometrically sharp features that can act as a breakdown precursor.

The results show that thermal stress induced by temperature rises of a few tens of Kelvin (which are typical of conditions caused by Joule heating in copper accelerator cavities) can significantly lower the electric fields needed for breakdown precursors to form compared to situations where such heating is absent (e.g., under dc field conditions). Our results show that diffusion-driven surface evolution can spontaneously create breakdown precursors in typically accessible regimes of applied fields and temperature rises for accelerator applications. Surface diffusion is therefore likely a viable candidate mechanism to explain the formation of sharp breakdown precursor in a broad range of conditions. Additional studies are, however, needed to understand how this mechanism interacts with other factors, including microstructural features such as grain boundaries, surface defects or impurities, or preexisting dislocations, which could possibly offer other favorable paths to the formation of BD precursors.

ACKNOWLEDGMENTS

R. S., S. B., E. S., and D. P. were supported by the Laboratory Directed Research and Development program of Los Alamos National Laboratory under Project No. 20230011DR. The work of S. B. was supported by the U.S. Department of Energy, Office of Science, Office of High Energy Physics under Award No. DE-SC0020429. Los Alamos National Laboratory is operated by Triad National Security, LLC, for the National Nuclear Security Administration of U.S. Department of Energy (Contract No. 89233218CNA000001).

[1] G. Teel, A. Shashurin, X. Fang, and M. Keidar, J. Appl. Phys. **121**, 023303 (2017).
[2] E. I. Simakov, V. A. Dolgashev, and S. G. Tantawi, Nucl. Instrum. Methods Phys. Res., Sect. A **907**, 221 (2018).
[3] C. Limborg-Deprey, C. Adolphsen, D. McCormick, M. Dunning, K. Jobe, H. Li, T. Raubenheimer, A. Vrielink, T. Vecchione, F. Wang, and S. Weathersby, Phys. Rev. Accel. Beams **19**, 053401 (2016).
[4] T. Lucas, X. Stragier, P. Mutsaers, and O. Luiten, Nucl. Instrum. Methods Phys. Res., Sect. A **1013**, 165651 (2021).
[5] J. H. Han, M. Krasilnikov, and K. Flöttmann, Phys. Rev. ST Accel. Beams **8**, 033501 (2005).
[6] A. Descoeudres, Y. Levinsen, S. Calatroni, M. Taborelli, and W. Wuensch, Phys. Rev. ST Accel. Beams **12**, 092001 (2009).
[7] A. Kyritsakis, M. Veske, K. Eimre, V. Zadin, and F. Djurabekova1, J. Phys. D **51**, 225203 (2018).
[8] K. Eimre, S. Parviainen, A. Aabloo1, F. Djurabekova, and V. Zadin, J. Appl. Phys. **118**, 033303 (2015).
[9] J. Wang and G. Loew, Field emission and rf breakdown in high-gradient room temperature linac structures, Stanford Linear Accelerator Center, SLAC Technical Report No. 7684, 1997.
[10] A. D. Cahill, J. B. Rosenzweig, V. A. Dolgashev, S. G. Tantawi, and S. Weathersby, Phys. Rev. Accel. Beams **21**, 102002 (2018).
[11] S. Döbert, rf breakdown in high frequency accelerators, SLAC National Accelerator Laboratory, Menlo Park, CA, Technical Report No. 10463, 2004.
[12] H. Zha and A. Grudiev, New CLIC-G structure design, Technical Report, CLIC-Note 1066, 2016.
[13] D. P. Pritzkau, rf pulsed heating, Ph.D. thesis, Stanford University, 2001.
[14] V. A. Dolgashev, L. Faillace, B. Spataro, S. Tantawi, and R. Bonifazi, Phys. Rev. Accel. Beams **24**, 081002 (2021).
[15] V. Dolgashev and S. Tantawi, Design of High Efficiency High Power Electron Accelerator System Based on Normal Conducting RF Technology for Energy and Environmental Applications. United States. https://doi.org/10.2172/1441166 (OSTI ID: 1441166).
[16] M. A. K. Othman, J. Picard, S. Schaub, V. A. Dolgashev, S. M. Lewis, J. Neilson, A. Haase, S. Jawla, B. Spataro, R. J. Temkin, S. Tantawi, and E. A. Nanni, Appl. Phys. Lett. **117**, 073502 (2020).
[17] S. Tantawi, M. Nasr, Z. Li, C. Limborg, and P. Borchard, Phys. Rev. Accel. Beams **23**, 092001 (2020).
[18] S. Bagchi, E. Simakov, and D. Perez, Front. Phys. **12**, 1353658 (2024).
[19] E. Z. Engelberg, A. B. Yashar, Y. Ashkenazy, M. Assaf, and I. Popov, Phys. Rev. Accel. Beams **22**, 083501 (2019).
[20] A. Pohjonen, F. Djurabekova, K. Nordlund, A. Kuronen, and S. Fitzgerald, J. Appl. Phys. **110**, 023509 (2011).
[21] S. Bagchi and D. Perez, Phys. Rev. Accel. Beams **25**, 033101 (2022).
[22] L. Laurent, S. Tantawi, V. Dolgashev, C. Nantista, Y. Higashi, M. Aicheler, S. Heikkinen, and W. Wuensch, Phys. Rev. ST Accel. Beams **14**, 041001 (2011).
[23] L. Anand and S. Govindjee, *Continuum Mechanics of Solids* (Oxford University Press, Oxford, United Kingdom, 2020).
[24] A. Boresi and R. Schmidt, *Advanced Mechanics of Materials*, 6th ed. (Wiley, Hoboken, NJ, 2002).
[25] W. Yang and D. Srolovitz, J. Mech. Phys. Solids **42**, 1551 (1994).
[26] W. Mullins, J. Appl. Phys. **28**, 333 (1957).
[27] M. Alnaes, J. Blechta, J. Hake, A. Johansson, B. Kehlet, A. Logg, C. Richardson, J. Ring, M. Rognes, and G. Wells, Arch. Numer. Software **3**, 9 (2015).
[28] R. C. Kirby and A. Logg, ACM Trans. Math. Softw. **32**, 417 (2006).
[29] A. Logg and G. N. Wells, ACM Trans. Math. Softw. **37**, 1 (2010).
[30] J. J. Hoyt, M. Asta, and A. Karma, Phys. Rev. Lett. **86**, 5530 (2001).
[31] H. J. Qian, C. Li, Y. C. Du, L. X. Yan, J. F. Hua, W. H. Huang, and C. X. Tang, Phys. Rev. ST Accel. Beams **15**, 040102 (2012).
[32] D. Srolovitz, Acta Metall. **37**, 621 (1989).
[33] D. Du and D. Srolovitz, Appl. Phys. Lett. **85**, 4917 (2004).
[34] V. G. Suvorov and N. M. Zubarev, J. Phys. D **37**, 289 (2003).
[35] D. Du and D. Srolovitz, Appl. Phys. Lett. **85**, 4917 (2004).
[36] V. Gill, P. Guduru, and B. Sheldon, Int. J. Solids Struct. **45**, 943 (2008).
[37] D. B. Butrymowicz, J. R. Manning, and M. E. Read, J. Phys. Chem. Ref. Data **2**, 643 (1973).
[38] L. Hansen, P. Stoltze, K. W. Jacobsen, and J. K. Nørskov, Phys. Rev. B **44**, 6523 (1991).
[39] M. Karimi, T. Tomkowski, G. Vidali, and O. Biham, Phys. Rev. B **52**, 5364 (1995).
[40] G. Schulze Icking-Konert, M. Giesen, and H. Ibach, Surf. Sci. **398**, 37 (1998).
[41] G. Kallinteris, G. Evangelakis, and N. Papanicolaou, Surf. Sci. **369**, 185 (1996).
[42] G. Evangelakis, D. Papageorgiou, G. Kallinteris, C. Lekka, and N. Papanicolaou, Vacuum **50**, 165 (1998).
[43] G. Evangelakis and N. Papanicolaou, Surf. Sci. **347**, 376 (1996).

[44] V. Kumykov, I. Sergeev, V. Sozaev, and M. Gedgagova, Bull. Russ. Acad. Sci. Phys. **81**, 357 (2017).

[45] N. Simon, E. Drexler, and R. P. Reed, Properties of copper and copper alloys at cryogenic temperatures, National Institute of Standards and Technology, Boulder, CO, final report, Technical Report, NIST monograph 177, 1992.

[46] A. Descoeudres, T. Ramsvik, S. Calatroni, M. Taborelli, and W. Wuensch, Phys. Rev. ST Accel. Beams **12**, 032001 (2009).